

Efficient and Accurate Graph Classification with Hyperdimensional Computing on FPGA

Jebacyril Arockiaraj
arockiar@usc.edu

University of Southern California
Los Angeles, USA

Dhruv Parikh
dhruvash@usc.edu

University of Southern California
Los Angeles, USA

Viktor Prasanna
prasanna@usc.edu

University of Southern California
Los Angeles, USA

Abstract

Real-time, energy-efficient inference on edge devices is essential for graph classification across a range of applications. Hyperdimensional Computing (HDC) is a brain-inspired computing paradigm that encodes input features into low-precision, high-dimensional vectors with simple element-wise operations, making it well-suited for resource-constrained edge platforms. Recent work enhances HDC accuracy for graph classification via Nyström kernel approximations. Edge acceleration of such methods faces several challenges: (i) redundancy among (landmark) samples selected via uniform sampling, (ii) storing the Nyström projection matrix under limited on-chip memory, (iii) expensive, contention-prone codebook lookups, and (iv) load imbalance due to irregular sparsity in SpMV.

To address these challenges, we propose **HyperX**, the first end-to-end FPGA accelerator for Nyström-based HDC graph classification at the edge. HyperX integrates four key optimizations: (i) a hybrid landmark selection strategy combining uniform sampling with determinantal point processes (DPPs) to reduce redundancy while *improving* accuracy; (ii) a streaming architecture for Nyström projection matrix maximizing external memory bandwidth utilization; (iii) a minimal-perfect-hash lookup engine enabling $O(1)$ key-to-index mapping; and (iv) sparsity-aware SpMV engines with static load balancing. Implemented on an AMD Zynq UltraScale+ (ZCU104) FPGA, **HyperX** achieves $6.85\times$ ($4.32\times$) speedup and $169\times$ ($314\times$) energy efficiency gains over optimized CPU (GPU) baselines, while *improving* classification accuracy by 3.4% on average across TUDataset benchmarks, a widely used standard for graph classification.

CCS Concepts

• **Hardware** → **Hardware accelerators**; • **Computer systems organization** → **Parallel architectures**.

Keywords

Hyperdimensional computing, Graph classification, FPGA acceleration, Edge intelligence, Sparse computation

ACM Reference Format:

Jebacyril Arockiaraj, Dhruv Parikh, and Viktor Prasanna. 2026. Efficient and Accurate Graph Classification with Hyperdimensional Computing on FPGA. In *Proceedings of the 23rd ACM International Conference on Computing*

Frontiers (CF '26), May 19–21, 2026, Catania, Italy. ACM, New York, NY, USA, 11 pages. <https://doi.org/10.1145/3801487.3801824>

1 Introduction

Graphs are a natural representation for capturing relationships between entities in diverse domains such as bioinformatics [6], chemistry [52], cybersecurity [17], and social network analysis [56]. Graphs exhibit irregular structure and variable size, making them difficult to process using conventional machine learning techniques. As a result, graph classification has emerged as a critical task and has received significant attention from the scientific community in recent years [14]. Graph classification assigns a label to an entire graph, such as a molecule or biological structure, based on its topology and node attributes. There is a growing demand to bring such capabilities onto the edge for applications such as molecular toxicity screening, wearable biochemical sensing [40, 44, 58], which require real-time decisions under limited energy budgets [48, 59].

Graph Neural Networks (GNNs) are a class of models that extend deep learning to graphs through techniques such as iterative message passing and neighborhood aggregation, achieving high accuracy in tasks such as graph classification. However, they incur significant computational and energy costs, making them less suitable for resource-constrained edge devices [30].

Hyperdimensional Computing (HDC) [22] is a brain-inspired computing paradigm that represents information using low-precision vectors, often comprising thousands of dimensions. Unlike deep neural networks, HDC does not require complex iterative training and often generalizes well with minimal data and computation, enabling applications such as biosignal analysis and cybersecurity [10, 15, 18, 25, 26, 32, 37, 60]. The lightweight, low complexity operations make HDC a compelling alternative to deep learning for low-power, real-time, and edge inference [24, 57].

A key step in HDC is feature encoding, which converts raw input features into hypervectors (HVs). Early graph-focused efforts [40] primarily captured graph topology and overlooked node attributes, limiting expressiveness. Recent work [58] addresses this by enabling kernel functions in the encoding stage, allowing HDC to capture complex, nonlinear graph structures. During inference, given an input graph, the model performs multi-hop propagation, generates integer codes for each node, hashes them into the codebook, and updates the query graph histogram. The histogram is then compared against landmark histograms to form a kernel score, which is projected via Nyström projection matrix into an HV for final classification.

By incorporating kernel methods into HDC encoding [58], the accuracy gap of HDC with GNN-based models for graph classification is significantly reduced. Despite the advantages, applying

arXiv:2512.08089v2 [cs.AR] 18 May 2026



This work is licensed under a Creative Commons Attribution 4.0 International License. *CF '26, Catania, Italy*

© 2026 Copyright held by the owner/author(s).
ACM ISBN 979-8-4007-2568-5/2026/05
<https://doi.org/10.1145/3801487.3801824>

this method at the edge raises several non-trivial challenges. First, general-purpose CPUs and GPUs are throughput-oriented and optimized for large-batch workloads, leading to poor utilization and high energy cost per query in edge inference. Second, the effectiveness of the Nyström method heavily depends on the diversity and number of landmark samples. The landmark count directly dictates the computational cost of kernel evaluations during inference and the associated memory footprint. Third, the inherent sparsity in the propagation kernel evaluation results in redundant operations, irregular memory access, and load imbalance across compute units. Fourth, the code-to-index lookup requires accessing hop-specific codebooks; these accesses are irregular and, when executed concurrently, they contend for memory access.

FPGAs are well-suited for HDC inference as they can exploit fine-grained parallelism and implement customized data paths. In this paper, we present the first FPGA accelerator for HDC-based graph classification, delivering real-time inference for edge deployment. The key contributions of this work are:

- We propose a novel sampling method that combines uniform sampling with DPP to reduce the number of redundant landmarks while preserving diversity, reducing kernel evaluation overhead and memory footprint, while *improving* accuracy.
- Guided by our roofline analysis, we develop a streaming architecture that maximizes external memory bandwidth utilization by issuing contiguous reads matching the memory-interface width and overlapping fetch and compute.
- We design a minimal-perfect-hash (MPH) engine that maps computed codes (keys) to query histogram indices in $O(1)$ time, enabling parallel histogram updates.
- We design SpMV processing elements (PEs) that exploit the sparsity in adjacency and landmark histogram matrices, reducing memory footprint and energy consumption. We employ a static load-balancing mechanism that partitions rows across PEs to reduce the load imbalance.
- Beyond the individual optimizations, we integrate them into **HyperX**, the first end-to-end FPGA accelerator for Nyström-based HDC graph classification at the edge, delivering real-time inference under tight memory and energy budgets.
- We implement our design on the AMD Zynq FPGA and evaluate it across benchmark datasets from TUDataset, a widely used standard for graph classification tasks. Our accelerator achieves $6.85\times$ ($4.32\times$) speedup and $169\times$ ($314\times$) energy efficiency over CPU (GPU) baselines, while improving classification accuracy by up to 3.4%, on average.

2 Preliminaries

2.1 Background

2.1.1 Hyperdimensional Computing (HDC). Hyperdimensional Computing (HDC) is a brain-inspired paradigm that represents information as high-dimensional vectors, or *hypervectors* (HVs), typically with dimensionality $d \sim 10^4$ [22, 27]. HVs are low-precision; in this work we assume bipolar HVs $\mathbf{h} \in \{-1, +1\}^d$. Representation learning in HDC utilizes a small set of inexpensive, element-wise operations, and noise-robust computations well-suited for hardware acceleration [19, 24]:

- **Bundling** (\oplus): element-wise addition and thresholding, e.g., $\mathbf{h} = \text{sign}(\mathbf{h}_1 + \mathbf{h}_2)$, to combine HVs while preserving similarity.
- **Binding** (\otimes): element-wise multiplication, $\mathbf{h} = \mathbf{h}_1 \odot \mathbf{h}_2$, to produce dissimilar HVs for encoding associations [42].
- **Permutation** (ρ): cyclic shift, $\rho^i(\mathbf{h}) = [h_{(j+i) \bmod d}]_{j=0}^{d-1}$, to encode position or sequence information [21].

An HDC classifier stores *class prototypes* as bundled HVs of training samples belonging to the same class. During inference, a query HV is compared against prototypes using a similarity metric, and the class with maximum similarity is predicted. HDC thus provides single-pass training [16], and hardware-friendly bit-level parallelism, making it attractive for edge-deployed learning systems [23, 47].

2.1.2 Nyström Encoding for HDC. Conventional HDC encodings rely on random projections [40, 43, 51], which fail to capture complex data similarity. The Nyström method [29, 54] provides a principled approach to approximate a positive semi-definite kernel $K(\cdot, \cdot)$ using a small set of $s \ll n$ *landmark* samples drawn from the training data of size n . This enables HDC to incorporate rich kernel-based similarity functions, such as the propagation kernel, significantly improving classification accuracy for graph classification tasks [58]. The propagation kernel [38] computes similarity between graphs by iteratively propagating node features through the adjacency matrix and comparing histograms of the propagated representations. In Nyström-HDC, this process produces hop-wise histogram features that are used to compute kernel similarities to landmark graphs. Specifically, each input x is represented by a kernel similarity vector $\mathbf{C}(x) \in \mathbb{R}^s$, which is projected into the hypervector space using a Nyström projection matrix $\mathbf{P}_{\text{nys}} \in \mathbb{R}^{d \times s}$, yielding a hypervector.

2.2 End-to-End Nyström-HDC Inference

As illustrated in Algorithm 1, given a query graph $G_x = (\mathbf{A}_x, \mathbf{F}_x)$, inference uses hop-specific codebooks $\{\mathcal{B}^{(t)}\}_{t=0}^{H-1}$, landmark histogram matrices $\{\mathbf{H}^{(t)}\}_{t=0}^{H-1}$ with $\mathbf{H}^{(t)} \in \mathbb{R}^{s \times |\mathcal{B}^{(t)}|}$ (row i is the hop- t histogram vector of landmark z_i computed during training), Locality Sensitive Hashing (LSH) parameters $\{(\mathbf{u}^{(t)}, b^{(t)})\}_{t=0}^{H-1}$ (with shared width $w > 0$), the Nyström projection matrix $\mathbf{P}_{\text{nys}} \in \mathbb{R}^{d \times s}$, and the class-prototype matrix $\mathbf{G} = [\mathbf{g}_1; \dots; \mathbf{g}_C] \in \{-1, +1\}^{C \times d}$, to encode G_x and classify it. At each hop, node features are propagated, node codes are computed in a vectorized fashion and binned (hashed) into a hop-specific histogram $\mathbf{h}^{(t)}$, which is then compared against all landmark histograms via a single matrix-vector product to yield a hop-wise similarity vector $\mathbf{v}^{(t)} \in \mathbb{R}^s$. Accumulating these over H hops produces the kernel-similarity vector $\mathbf{C} \in \mathbb{R}^s$, which is embedded to an HV and matched to class prototypes.

2.3 Problem Definition

Given a labeled graph dataset $\mathcal{D} = \{(G_i, y_i)\}_{i=1}^n$ with $G_i = (\mathbf{A}_i, \mathbf{F}_i)$ and labels $y_i \in \{1, \dots, C\}$, *graph classification* seeks a mapping $f : (\mathbf{A}, \mathbf{F}) \mapsto \{1, \dots, C\}$. At inference, a query graph $G_x = (\mathbf{A}_x, \mathbf{F}_x)$ is assigned label $\hat{y} = f(\mathbf{A}_x, \mathbf{F}_x)$. We specifically target *single-graph, real-time* Nyström-HDC inference on resource-constrained FPGAs.

Algorithm 1 End-to-End Inference for Nyström-HDC

Require: $\mathbf{A}_x \in \{0, 1\}^{N \times N}$; $\mathbf{F}_x \in \mathbb{R}^{N \times f}$; hops H ; codebooks $\{\mathcal{B}^{(t)}\}$; landmark histograms $\{\mathbf{H}^{(t)} \in \mathbb{R}^{s \times |\mathcal{B}^{(t)}|}\}$; LSH params $\{(u^{(t)}, b^{(t)})\}$ and width w ; Nyström projection $\mathbf{P}_{\text{nys}} \in \mathbb{R}^{d \times s}$; class prototypes $\mathbf{G} \in \{-1, +1\}^{C \times d}$

Ensure: Query HV $\mathbf{h} \in \{-1, +1\}^d$ and predicted class \hat{y}

- 1: $\mathbf{M} \leftarrow \mathbf{F}_x$ ▷ node features
- 2: $\mathbf{C} \leftarrow \mathbf{0} \in \mathbb{R}^s$ ▷ similarity accumulator
- 3: **for** $t = 0$ **to** $H - 1$ **do**
- 4: $\mathbf{c} \leftarrow \left\lfloor (\mathbf{M}u^{(t)} + b^{(t)}\mathbf{1}_N) / w \right\rfloor \in \mathbb{Z}^N$ ▷ LSH codes
- 5: $\mathbf{h}^{(t)} \leftarrow \mathbf{0} \in \mathbb{Z}^{|\mathcal{B}^{(t)}|}$ ▷ histogram
- 6: **for** $v = 1$ **to** N **do**
- 7: $\mathbf{c} \leftarrow \mathbf{c}[v]$
- 8: **if** $\mathbf{c} \in \mathcal{B}^{(t)}$ **then** $j \leftarrow \text{INDEX}(\mathcal{B}^{(t)}, \mathbf{c})$; $\mathbf{h}^{(t)}[j] \leftarrow \mathbf{h}^{(t)}[j] + 1$
- 9: $\mathbf{v}^{(t)} \leftarrow \mathbf{H}^{(t)}\mathbf{h}^{(t)} \in \mathbb{R}^s$ ▷ hop similarity
- 10: $\mathbf{C} \leftarrow \mathbf{C} + \mathbf{v}^{(t)}$ ▷ accumulating into kernel similarity vector
- 11: **if** $t < H - 1$ **then**
- 12: $\mathbf{M} \leftarrow \mathbf{A}_x \mathbf{M}$ ▷ propagate
- 13: $\mathbf{y} \leftarrow \mathbf{P}_{\text{nys}} \mathbf{C} \in \mathbb{R}^d$; $\mathbf{h} \leftarrow \text{sign}(\mathbf{y})$ ▷ encoding
- 14: $\hat{y} \leftarrow \arg \max_{c \in \{1, \dots, C\}} \text{sim}(\mathbf{h}, \mathbf{g}_c)$ ▷ similarity against class prototypes
- 15: **return** \mathbf{h} and \hat{y}

For each query graph, we measure energy per graph (mJ) and end-to-end latency (ms) from input arrival to prediction. The goal is to minimize both metrics while operating within the constraints of on-chip memory (BRAM/URAM), compute fabric (LUTs, DSPs), and external memory bandwidth (DDR), thereby enabling real-time Nyström-HDC graph classification on edge platforms.

We summarize the computational complexity of the operations in Algorithm 1 in Table 1. The table highlights that the per-graph cost is dominated by repeated propagation, codebook lookup, and landmark similarity computations across H hops, along with one-time costs from Nyström projection and prototype matching. Note that ϕ_A and $\phi_{H^{(t)}}$ refer to the average per-row density of the sparse matrices: adjacency matrix \mathbf{A} and landmark histogram matrix $\mathbf{H}^{(t)}$.

Table 1: Computational complexity of end-to-end Nyström-HDC inference for one query graph.

Operation	Expression	Repetition	Complexity
Feature Propagation	$\mathbf{M} \leftarrow \mathbf{A}\mathbf{M}$	$H-1$	$2\phi_A N^2 f$
LSH Code Generation	$(\mathbf{M}u^{(t)} + b^{(t)}\mathbf{1}_N) / w$	H	$2Nf$
Codebook Lookup	$\mathbf{c}^{(t,i)} \in \mathcal{B}^{(t)}$	H	$N \log \mathcal{B}^{(t)} $
Landmark Similarity	$\mathbf{v}^{(t)} = \mathbf{H}^{(t)}\mathbf{h}^{(t)}$	H	$2\phi_{H^{(t)}} \mathcal{B}^{(t)} s$
Nyström Projection	$\mathbf{y} = \mathbf{P}_{\text{nys}} \mathbf{C}$	1	$2sd$
Prototype Matching	$\text{sim}(\mathbf{h}, \mathbf{g}_c)$	1	$2Cd$
Argmax	$\arg \max_c$	1	C
Total			$2(H-1)\phi_A N^2 f + 2HNf + N \sum_{t=0}^{H-1} \log \mathcal{B}^{(t)} + 2s \sum_{t=0}^{H-1} \phi_{H^{(t)}} \mathcal{B}^{(t)} + 2sd + 2Cd + C$

3 Challenges and Key Innovation

We summarize the key challenges and our innovations in accelerating Algorithm 1 on resource-constrained edge platforms.

Challenge #1 – High redundancy in landmark samples. Nyström-based HDC selects landmarks via uniform sampling [58], giving every training graph an equal probability of being selected as a landmark. This often yields structurally similar landmarks, leading

to redundancy. Since each query graph is compared against all landmarks during inference, this redundancy increases memory footprint and computation, scaling with $O(sd)$. **Our innovation:** A hybrid Uniform + DPP sampling strategy (offline) that maintains landmark diversity during selection (Section 4.1, 6.5.3).

Challenge #2 – Large projection matrix size. The Nyström projection matrix dominates model parameters and exceeds on-chip memory capacity on edge FPGAs (e.g., ZCU104 provides ~4.5 MB versus 7–16 MB required). Consequently, the matrix must be streamed from off-chip DDR during inference with limited external memory bandwidth. **Our innovation:** Guided by our roofline analysis (Section 5.2.5), we design a streaming architecture that maximizes external memory bandwidth (Section 5.2.5).

Challenge #3 – Expensive codebook lookup. For every node and hop, the code must be mapped through a hop-specific codebook to locate its histogram bin. Naïve implementations require repeated dictionary searches, which scale poorly and introduce conflicts when many nodes are processed in parallel. **Our innovation:** We design a novel lightweight MPH-based lookup engine that delivers constant-time $O(1)$ code-to-index mapping, by banking both hash tables and codebook, minimizing conflicts (Section 5.2.2).

Challenge #4 – Severe load imbalance in SpMV. Sparse matrix operations such as feature propagation (via \mathbf{A}) and landmark histogram similarity computation (via $\mathbf{H}^{(t)}$) can become bottlenecks despite their low computational cost. Irregular row sparsity often leaves some PEs idle while others stall on dense rows, leading to severe under-utilization of compute resources. **Our innovation:** We employ a static load balancing strategy based on precomputed schedule tables (Section 4.2), eliminating under-utilization.

4 Optimizations

4.1 Landmark Reduction via DPP Sampling

An important step in Nyström-based HDC encoding [58] is the selection of landmark graphs [31]. These landmarks serve as the representative subset used to construct the Nyström projection matrix, and during inference, every query graph must be compared against the landmarks. The diversity of this landmark set, therefore, directly affect both the computational cost and the classification accuracy. Baseline approaches often rely on random uniform sampling [54], which does not guarantee diversity. As a result, graphs with a similar structure and node features may repeatedly be chosen as landmarks, increasing the projection cost while reducing accuracy due to bias toward certain structures. To address this, we adopt a diversity-aware selection method based on Determinantal Point Processes (DPPs) [28]. DPPs favor subsets with high pairwise dissimilarity, thereby improving diverse landmark coverage.

Unlike prior works [31], which target Euclidean data, where kernel evaluations reduce to dot products or distance computations, graph similarity requires propagation kernel [38] evaluations that are substantially more expensive. Consequently, constructing the DPP kernel requires all pairwise kernel evaluation, and the DPP sampling further incurs eigen decomposition cost $O(s^3)$. Thus, applying DPP directly to all training graphs is impractical. Therefore, we adopt a hybrid Uniform+DPP strategy that first reduces the candidate pool to a maximum of 300 graphs, or 2% of the training set, as in [58] with uniform sampling, and then applies DPP.

Algorithm 2 Hybrid Landmark Selection with DPP**Require:** Graph set \mathcal{G} , target landmark count s **Ensure:** Landmark set \mathcal{L}

- 1: Draw candidate pool $C \subset \mathcal{G}$ using uniform sampling
- 2: Compute similarity kernel K over C using the propagation kernel
- 3: Apply DPP sampling on K to select s diverse landmarks
- 4: **return** \mathcal{L}

This strategy retains the diversity benefits of DPP while keeping the landmark selection cost during training manageable. The impact is twofold. First, fewer redundant landmarks reduce the dimensionality s of the Nyström projection matrix $\mathbf{P}_{\text{nys}} \in \mathbb{R}^{d \times s}$, which directly lowers both computation and memory usage. Second, the improved diversity of landmarks enhances classification accuracy by reducing the overrepresentation of similar graph patterns. These benefits make DPP-based landmark selection a practical optimization for deploying Nyström-HDC [58] on edge FPGAs.

4.2 Static Load Balancing

Irregular sparsity in adjacency matrices (\mathbf{A}) and landmark histograms ($\mathbf{H}^{(t)}$) can cause severe PE underutilization. To avoid runtime scheduling overhead while maintaining balanced utilization, we design a lightweight *static iteration-wise load balancer* that maps rows to PEs offline, ensuring all PEs remain evenly loaded.

Schedule table. Given N rows and P PEs, computation proceeds in N/P iterations. In each iteration, every PE processes exactly one row, with assignments specified by a precomputed $N/P \times P$ *schedule table*. Each row of the table corresponds to one iteration, and each column to a PE; entry (i, j) gives the row index assigned to PE j in iteration i . The table is banked along columns, allowing PEs to fetch their assigned rows concurrently without conflict. At runtime, PE j fetches its row index, reads `row_ptr` and `col_idx/val` from Compressed Sparse Row (CSR) banks, and accumulates results directly into `out[row_id]`.

Offline construction. The table is constructed once per sparse operand using a simple nonzero-count grouping procedure: (1) Compute `nnz[r]` number of non-zero elements in each row; (2) Bucket rows into lists keyed by `nnz`; (3) Traverse buckets in increasing order of `nnz`, greedily allocating P rows at a time to form one iteration. If a bucket contains fewer than P rows, allocation continues with the next bucket until P rows are obtained. This procedure groups rows with similar sparsity into the same iteration, yielding balanced PE utilization at each cycle. It runs in $O(N)$ time, preserves the CSR layout, and produces a compact schedule table stored in BRAM.

Execution. At runtime, the controller issues iterations sequentially. Each PE reads its row index from the schedule table, performs CSR expansion, and writes directly to `out[row_id]`, with no dynamic scheduling or reassignment required.

5 Accelerator Design

5.1 HyperX Overview

Figure 1 shows the overview of **HyperX**, our FPGA accelerator for Nyström-HDC graph classification. **HyperX** is composed of six compute engines: (i) the Locality Sensitive Hashing Unit (LSHU),

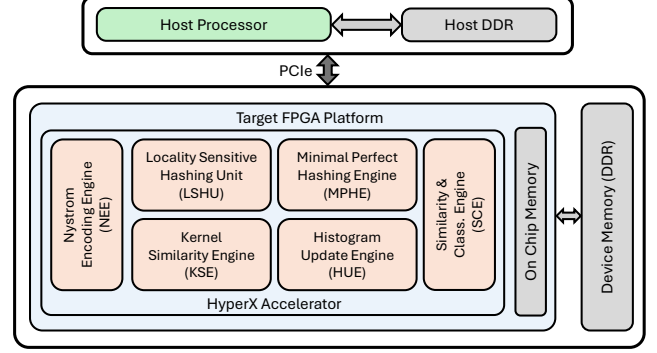


Figure 1: Overview of the HyperX FPGA accelerator.

which generates integer codes for nodes at each hop; (ii) the Minimal Perfect Hashing Engine (MPHE), which maps integer codes to valid histogram indices in $O(1)$ time using a MPH; (iii) the Histogram Update Engine (HUE), which accumulates counts into hop-specific histograms using the indices from MPHE; (iv) the Kernel Similarity Engine (KSE), which computes landmark similarities by multiplying the query histogram with buffered landmark histograms; (v) the Nyström Encoding Engine (NEE), which projects the kernel vector into the hyperdimensional space; and (vi) the Similarity & Classification Engine (SCE), which computes final class scores by comparing the encoded hypervector against class prototypes, followed by argmax selection of the label.

5.2 Architectural Components

5.2.1 Locality Sensitive Hashing Unit (LSHU). The LSHU is responsible for generating hop-specific codes. As depicted in Algorithm 1, Nyström-HDC inference first computes the locality sensitive hash $\lfloor \frac{\mathbf{M}\mathbf{u} + b\mathbf{1}_N}{w} \rfloor$, where $\mathbf{M} = \mathbf{F}_x$ initially, and then propagates $\mathbf{M} \leftarrow \mathbf{A}\mathbf{M}$, to generate code vector \mathbf{c} . This requires storing intermediate feature matrices of size $O(Nf)$. In our implementation, we restructure this computation into a sequence of matrix-vector products, computed via LSHU. Specifically, we first compute the projection $\mathbf{c} = \mathbf{F}_x\mathbf{u}$. Next, we iterate over the hop count to compute $\mathbf{c} \leftarrow \mathbf{A}\mathbf{c}$. This computes the required $\mathbf{M}^{(k)}\mathbf{u}^{(k)}$ as $\mathbf{A}^k\mathbf{F}_x\mathbf{u}^{(k)}$. While both methods require access to \mathbf{F}_x , the baseline requires storing the full feature matrix $\mathbf{M}^{(k)} \in \mathbb{R}^{N \times f}$ as opposed to the intermediate vectors of length N required by our restructuring, significantly reducing the on-chip memory resources required during code generation. In terms of complexity, the baseline requires $HNf + (H-1)f \text{nnz}(\mathbf{A}_x)$ operations, whereas our restructuring reduces this to $HNf + \frac{H(H-1)}{2} \text{nnz}(\mathbf{A}_x)$. This offers a clear advantage when $f > H/2$, which typically holds since hop counts are small ($H \leq 10$) while feature dimensions are much larger (e.g., $f \approx 50$).

Real-world graphs are sparse [40], and the LSHU exploits this by storing \mathbf{A} in CSR format and skipping zero entries, thereby reducing both the compute and memory bandwidth demand – critical under edge constraints. However, irregular sparsity causes load imbalance across PEs. To mitigate this, we employ *static schedule tables* (Section 4.2), which pre-assign rows to PEs based on nonzero counts, ensuring balanced utilization without runtime scheduling overhead. Figure 2 summarizes the architecture. The DenseMV unit

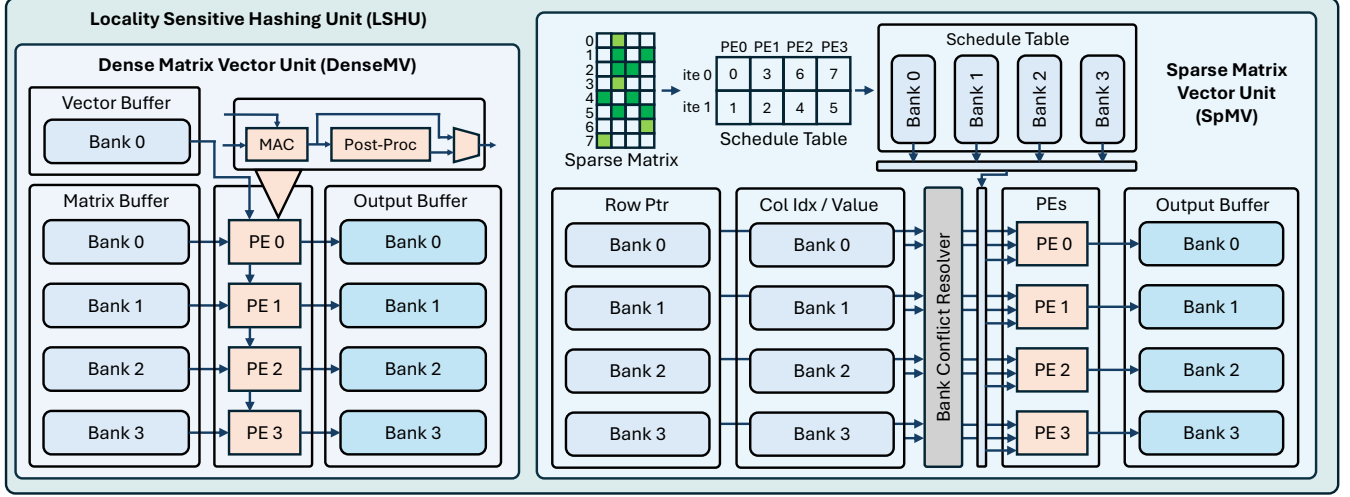


Figure 2: Locality Sensitive Hashing Unit (LSHU). It integrates a DenseMV unit (for F_u) and a SpMV unit (for A_c), with schedule tables, CSR arrays, and output buffers banked across BRAMs; a bank conflict resolver manages access overlaps, enabling concurrent output computation.

performs feature projection, while the SpMV unit handles hop-wise propagation. For SpMV, schedule tables are banked and accessed concurrently by all PEs, enabling each PE to fetch its assigned rows in parallel. CSR arrays (`row_ptr`, `col_idx`, `val`) and outputs are also banked across BRAMs to reduce contention, with conflicts managed by a bank conflict resolver. Each PE includes a dedicated MAC unit with a private accumulator and writes results directly to its assigned output index, enabling parallel and energy-efficient sparse computation.

5.2.2 Minimal Perfect Hashing Engine (MPHE). We adopt a MPH scheme [33] to map codes (keys) in the codebook to indices $\{0, \dots, |\mathcal{B}^{(t)}| - 1\}$ with $O(1)$ query time during inference. The scheme constructs the MPH as a cascade of levels A_0, A_1, \dots , where each bit-array A_d is sized to balance memory against collision probability. During construction, keys hashing uniquely at level d set a 1 at position $h_d(\text{key})$ and are removed, while colliding keys advance to the next level $d+1$. The final structure concatenates all bit-arrays with a lightweight *rank* vector. At query time, a key traverses the levels until it encounters a 1, and its index is computed as the cumulative number of 1s preceding that position. This yields a compact (≈ 3 bits/key) structure supporting constant-time queries. The MPHE performs inference-time dictionary lookup from code \rightarrow histogram index. Upstream, the LSHU produces a chunk of integer codes, which are enqueued into a *lookup queue*. Each lookup then proceeds as follows:

- (1) *Hash generation.* A *Hash Function Engine* computes two 64-bit hashes for the input code using a seeded integer hash function [53]. The level- d probe index is $i_d \leftarrow h_d(\text{code}) \bmod |A_d|$, where $|A_d|$ is the bit capacity of level table A_d .
- (2) *Level table probe.* Level tables $\{A_d\}$ are stored on-chip as banks of 64-bit words; the bit at i_d is checked within its word. If it is 0, the code advances to the next level by generating the next hash in the sequence via a xorshift-based rehash generator [49].

- (3) *Rank to MPH index.* On a 1-bit hit at (d, i_d) , the engine retrieves the global index directly from the rank vector. Each entry in the rank vector stores the cumulative number of 1s up to the start of a word, aggregated across all levels. The final index is obtained by adding this value to the popcount of bits within the current word up to (and including) position i_d , and subtracting one for zero-based indexing.
- (4) *Codebook verification.* The MPH index addresses a compact *codebook store* that holds pairs $(\text{code}, \text{hist_idx})$. The queried code is compared against the stored code. If they match, the corresponding `hist_idx` is emitted as valid. If they differ, the lookup terminates, as a hit with a mismatch implies the queried code is not in the original codebook. If all levels are probed with no hit, the code is deemed absent. No histogram update occurs for a queried code absent from the codebook.

Figure 3 illustrates the MPHE datapath: (a) a *Lookup Queue* collects codes from LSHU PEs; (b) a *Hash Function Engine* generates 64-bit hashes and level indices; (c) *Level Tables* A_d and *Rank Vectors*, each banked across BRAMs, are accessed in parallel; (d) an *Index Buffer* carries the computed MPH index; and (e) a banked *Codebook* returns the $(\text{code}, \text{hist_idx})$ pair to a *Compare Unit* that verifies code presence. Level tables and rank vectors are placed in independent banks to support pipelined parallel lookups (Figure 3), while contention in codebook access is reduced through MPH hashing, pipelining, and banking. The pipeline roughly issues one index lookup per cycle, with $O(1)$ cost bounded by the small number of level tables per codebook.

5.2.3 Histogram Update Engine (HUE). The HUE maintains hop-specific query histogram vector $\mathbf{h}^{(t)}$, incrementing it based on the indices returned by MPHE. To maximize update parallelism, each PE in HUE keeps a private copy of the histogram, allowing concurrent increments without contention. Once all codes in the current hop are processed, local histograms are merged into the global hop histogram through a reduction step. This two-stage

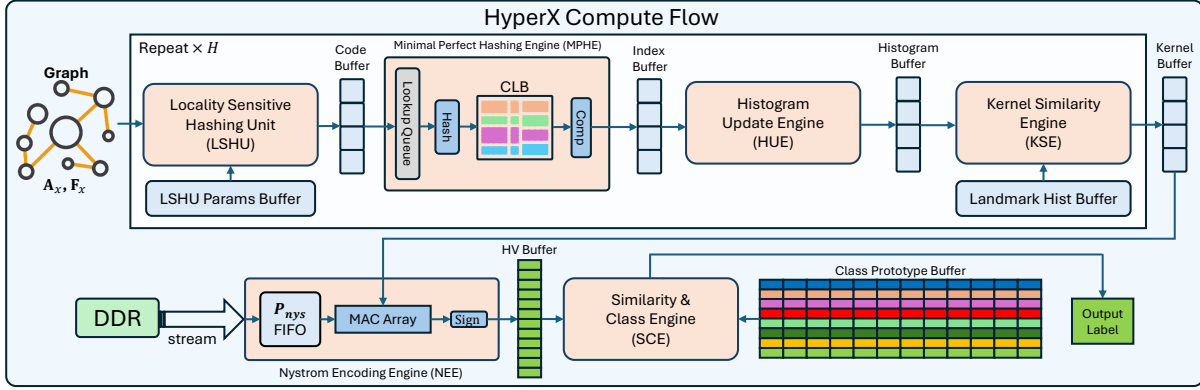


Figure 5: HyperX compute flow across hops: input graph $\{A_x, F_x\}$ is processed by compute engines to produce class label.

HUE, where PEs increment local histograms in parallel before merging into the hop-global histogram buffer. Once a hop histogram is complete, the *KSE* multiplies it with pre-stored landmark histograms. Implemented as a SpMV, this step accumulates partial results into the global kernel similarity vector C . After all hops finish, the *NEE* consumes C from the kernel buffer. The projection matrix P_{nys} is streamed from DDR through a FIFO into the MAC array, where they are multiplied with the corresponding elements of C to generate the output hypervector. The $\text{sign}()$ function is fused directly into the MAC array, producing a bipolarized HV on the fly. Finally, the *SCE* computes class scores by multiplying the encoded hypervector with class prototypes, followed by an argmax to select the label.

6 Experimental Evaluation

6.1 Implementation Details

We implement the proposed accelerator on an AMD Zynq Ultra-Scale+ ZCU104 FPGA [4], representative of an edge-class FPGA. The accelerator is designed using AMD Vitis High Level Synthesis (HLS) and synthesized using AMD Vitis Unified IDE v2024.2 [2]. We instantiate 4 PEs in the LSHU, KSE, and HUE compute engines of the accelerator to conserve on-chip resources (LUT/DSP/BRAM) for the NEE compute engine, which dominates area and latency. Empirically, configurations with more than 4 PEs result in marginal speedup while increasing resource usage, so 4 PEs remain the best end-to-end trade-off on ZCU104. For NEE, P_{nys} is streamed through a 512-bit AXI transfer width. This width is selected because Vitis HLS automatically widens burst ports up to 512 bits [3] and AXI SmartConnect inserts width converters to match the platform’s native memory ports [1]. For a 32-bit precision, each transfer packs 16 FP32 values and drives 16 parallel MAC lanes. We employ a 512-entry, 16-FP32-wide stream FIFO to overlap data fetch and compute. Table 2 reports the resource utilization obtained through the Vitis Unified IDE, with an achieved frequency of 300 MHz.

6.2 Datasets

We evaluate on eight benchmark datasets from the TUDataset [36], a widely used collection for graph classification, consistent with prior work on HDC-based graph classification [40, 58]. These

Table 2: Resource Utilization of the Proposed Design

Resource	Used	Available	Utilization
LUT	71,900	230,400	31%
FF	87,800	460,800	19%
BRAM (18K)	329	624	52%
DSP	156	1,728	9%
URAM	0	96	0%

datasets span diverse domains (e.g., bioinformatics, chemistry, and drug discovery) and vary in graph sizes and structures, providing a representative set for evaluating **HyperX**. Importantly, graph classification benchmarks consist of many independent graphs whose sizes are inherently bounded by the application domain; large single-graph workloads (e.g., citation networks) are characteristic of node classification and are not representative of this task. Table 3 summarizes the dataset statistics.

Table 3: Summary of Graph Classification Datasets

Task	#Train	#Test	Avg. Nodes	Avg. Edges	Description
ENZYMES [6]	480	120	33	62	Protein graphs
NCI1 [52]	3288	822	30	32	Chemical compounds
D&D [12]	943	235	284	716	Protein structures
BZR [50]	324	81	36	38	Drug activity graphs
MUTAG [11]	150	38	18	20	Mutagenicity prediction
COX2 [50]	373	94	41	43	Drug activity graphs
NCI109 [52]	3301	826	30	32	Chemical compounds
Mutagenicity [45]	3469	868	30	31	Mutagenicity prediction

6.3 Baseline Platforms

We evaluate our FPGA accelerator against CPU and GPU baselines: the AMD Ryzen 5 5625U and the NVIDIA RTX A4000. All baselines are implemented in PyTorch (v2.4.1) with Python 3.8 and CUDA 12.1. We select the Ryzen processor as representative of CPUs deployed in laptops and compact systems, while the RTX A4000 is a workstation-class GPU commonly used as a baseline in prior HDC works [7, 8, 13, 34]. Both baselines offer substantially higher peak compute and memory resources than our target edge FPGA, providing a conservative comparison. For fairness, GPU latency is measured after all model parameters are transferred to device memory. This favors the GPU, which benefits from high-bandwidth GDDR6 memory, whereas on the FPGA, the Nyström projection

Table 4: Specifications of Baseline Platforms

	CPU	GPU	FPGA (Ours)
Platform	AMD Ryzen 5 5625U	NVIDIA RTX A4000	AMD ZCU104
Frequency	2.3 GHz (base)	1560 MHz	300 MHz
Peak Perf.	2.4 TFLOPS (FP32)	19.2 TFLOPS (FP32)	0.26 TFLOPS (FP32)
On-chip Mem.	3 MB L2, 16 MB L3	6 MB L2 Cache	4.5 MB
Memory BW	50 GB/s (DDR4)	448 GB/s (GDDR6)	19.2 GB/s (DDR4)

Table 5: End-to-end latency (ms) per graph. Speedup in parentheses is relative to the CPU baseline (without DPP).

Dataset	CPU	CPU+DPP	GPU	GPU+DPP	FPGA	FPGA+DPP
DD	7.47 (1.00x)	6.11 (1.22x)	3.00 (2.49x)	3.00 (2.49x)	1.80 (4.15x)	1.65 (4.53x)
ENZYMES	4.71 (1.00x)	2.55 (1.85x)	1.77 (2.66x)	1.60 (2.94x)	0.61 (7.72x)	0.45 (10.47x)
MUTAG	5.13 (1.00x)	3.87 (1.33x)	5.80 (0.88x)	4.90 (1.05x)	1.47 (3.49x)	1.19 (4.31x)
NCI1	5.04 (1.00x)	4.23 (1.19x)	2.70 (1.87x)	2.60 (1.94x)	0.98 (5.14x)	0.61 (8.26x)
BZR	2.85 (1.00x)	2.29 (1.24x)	1.70 (1.67x)	1.60 (1.78x)	0.54 (5.27x)	0.32 (8.89x)
COX2	5.26 (1.00x)	4.68 (1.12x)	7.30 (0.72x)	6.70 (0.79x)	1.45 (3.63x)	1.05 (5.01x)
NCI109	4.26 (1.00x)	3.44 (1.24x)	2.50 (1.70x)	2.60 (1.64x)	1.07 (3.98x)	0.69 (6.17x)
Mutagenicity	3.57 (1.00x)	3.01 (1.19x)	1.80 (1.98x)	1.70 (2.10x)	0.79 (4.52x)	0.50 (7.13x)

matrix—the dominant model parameter—must be streamed from DDR during inference. Despite this, **HyperX** consistently achieves lower latency. While workstation-class GPUs naturally draw more power, we report energy efficiency (mJ/graph) to ensure fairness.

6.4 Evaluation Metrics

We report four key metrics: (i) *Classification accuracy* (%): fraction of correctly predicted labels against ground truth; (ii) *Latency* (ms/graph): average end-to-end inference time per graph at batch size 1, measured from the arrival of the graph’s adjacency and feature matrices to the prediction of class label; (iii) *Power* (W): average device power during steady-state inference, including static and dynamic components; (iv) *Energy Efficiency* (mJ/graph): average energy per inference, computed as the product of measured power and latency.

6.5 Results and Analysis

6.5.1 Latency. For FPGA, cycle-accurate latency is obtained from the integrated analyzer in the AMD Vitis Unified IDE v2024.2. CPU and GPU latencies are measured using wall-clock timing in PyTorch with batch size set to one, consistent with real-time edge inference. Table 5 summarizes the results, across all datasets, **HyperX** consistently delivers lower latency than CPU and GPU baselines, despite both being more resource-rich and compute-capable. On average, FPGA latency is reduced by 4.5× relative to CPU and 2.2× relative to GPU. The low latency is due to the FPGA-specific optimizations, such as streaming dataflow to decouple DDR from compute and BRAM-banked on-chip memory for conflict-free memory access. DPP further reduces per-inference latency by 25 to 40% by pruning redundant landmarks, which reduces memory transfers of P_{nys} .

6.5.2 Energy Efficiency. Table 6 compares throughput, power, and energy efficiency across platforms. CPU power is measured with a plug-in power meter, model PM01-US, GPU power using the nvidia-smi [41] command line tool, and FPGA power from the AMD Vitis Unified IDE [2] post-implementation, consistent with standard FPGA power estimation [47]. Table 6 reports that our FPGA design delivers orders of magnitude lower energy per graph over CPU and GPU baselines, while also increasing throughput. Across the TU datasets, the FPGA energy is 101× to 256× lower

Table 6: Throughput, power, and energy efficiency with DPP on TU datasets. Energy ratios are normalized to FPGA (=1×).

Dataset	Device	Throughput (graphs/s)	Power (W)	Energy Efficiency (mJ/graph)
DD	CPU	163	25.2	154 (116×)
	GPU	333	59.0	177 (133×)
	FPGA	606	0.81	1.33 (1×)
Enzymes	CPU	392	24.3	62 (194×)
	GPU	625	61.0	98 (305×)
	FPGA	2222	0.71	0.32 (1×)
Mutag	CPU	259	25.3	98 (101×)
	GPU	204	60.0	294 (303×)
	FPGA	840	0.81	0.97 (1×)
NCI1	CPU	236	25.5	108 (225×)
	GPU	385	61.0	159 (330×)
	FPGA	1639	0.79	0.48 (1×)
BZR	CPU	437	24.6	56 (256×)
	GPU	625	62.0	99 (451×)
	FPGA	3125	0.70	0.22 (1×)
COX2	CPU	214	24.4	114 (127×)
	GPU	149	61.0	409 (454×)
	FPGA	952	0.86	0.90 (1×)
NCI109	CPU	291	24.9	86 (156×)
	GPU	385	60.0	156 (284×)
	FPGA	1449	0.79	0.55 (1×)
Mutagenicity	CPU	332	24.4	73 (184×)
	GPU	588	60.0	102 (255×)
	FPGA	2000	0.79	0.40 (1×)

than CPU and 133× to 451× lower than GPU. These improvements arise from our architectural choices, such as DPP-based landmark reduction, bandwidth-aware streaming of P_{nys} .

6.5.3 Impact of DPP on Accuracy and Memory. Figure 6 reports classification accuracy across eight TU datasets [36], comparing **HyperX** against state-of-the-art HDC baselines GraphHD [40] and NysHD [58]. GraphHD results are taken from prior work [40, 58], and we re-implement [58] using the authors’ open-source repository under identical experimental settings. Our design improves accuracy by 3.4% on average over NysHD. We outperform both baselines on six of eight datasets; on COX2 and Mutag, GraphHD performs slightly better. This behavior reflects our hybrid uniform+DPP landmark selection. Uniform sampling introduces randomness and redundancy, which can have a significant impact on small datasets. A full DPP-based sampling could reduce this impact, but it is computationally expensive due to eigendecomposition and full kernel matrix construction. Our hybrid approach preserves most of DPP’s diversity benefits at a lower sampling cost. Beyond accuracy, DPP reduces the memory required for model parameters in Algorithm 1. Table 7 shows that by eliminating redundant landmarks, DPP-based landmark reduction lowers total memory required by 37% on average.

6.5.4 Impact of Load Balancing (LB). We quantify the benefit of the static, offline row scheduling in Section 4.2 by comparing FPGA latency with and without load balancing. Figure 7 reports speedup normalized to the *no-LB* case (=1). Across the TU datasets, we observe consistent gains of 1.19× on average. Datasets with broader per-row nnz variance (e.g., DD, COX2) benefit the most, due to reduced PE idling and fewer BRAM-port stalls.

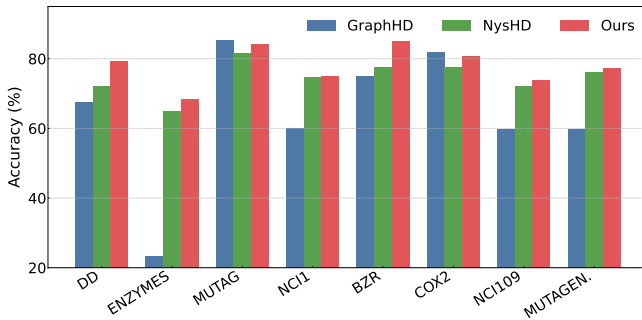


Figure 6: Classification accuracy (%) on TU datasets.

Table 7: Memory consumption of model parameters.

Dataset	Memory w/o DPP (MB)	Memory w/ DPP (MB)
DD	12.50	9.15 (↓ 26.8%)
Enzymes	16.13	11.13 (↓ 31.0%)
Mutag	7.49	4.62 (↓ 38.3%)
NCI1	12.54	7.88 (↓ 37.2%)
BZR	11.78	7.02 (↓ 40.4%)
COX2	12.50	7.70 (↓ 38.4%)
NCI109	12.50	6.97 (↓ 44.2%)
Mutagenicity	11.86	7.16 (↓ 39.6%)

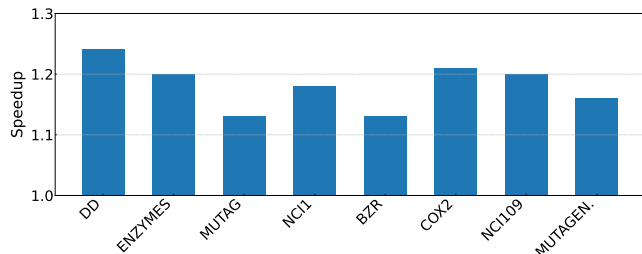


Figure 7: Effect of static load balancing in SpMV stages (LSHU/KSE): Speedup normalized to no LB case (=1).

Table 8: Memory overhead of MPHE metadata.

Dataset	Hops	MPH Metadata	Codebook (KB)	Total (KB)	Overhead
DD	2	490 B (392 B / 98 B)	4.63	5.11	10.3%
Mutagenicity	3	330 B (264 B / 66 B)	2.48	2.80	13.0%
MUTAG	10	1.88 KB (1.50 KB / 384 B)	18.41	20.29	10.2%
NCI109	5	840 B (672 B / 168 B)	7.49	8.31	10.9%

6.5.5 Ablations Studies. Figure 8 isolates the impact of the NEE by comparing end-to-end FPGA inference latency with and without NEE optimizations. The results show that without streaming dataflow, FIFO buffering, or 512-bit-aligned DDR access, inference latency is dominated by stalled memory accesses. Figure 8 evaluates the impact of the MPHE by comparing it with an optimized binary-search-based codebook lookup. The results highlight our design choice of a fully pipelined $O(1)$ key-to-index mapping. MPHE introduces a small amount of auxiliary metadata to enable constant-time, conflict-free codebook lookup reported in Table 8. Even in the largest configuration (MUTAG, 10 hops), the combined MPHE metadata and codebook size is only 20.29 KB (0.16 Mb), which constitutes a negligible fraction of available on-chip memory.

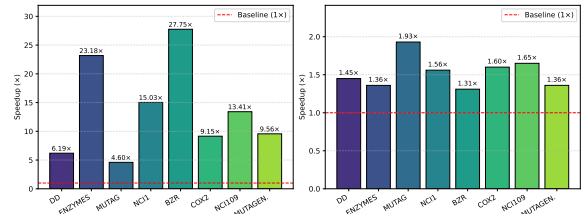


Figure 8: Ablation study showing speedup over baseline: (left) NEE ablation and (right) MPHE ablation.

7 Related Works

Graph Classification with HDC: GraphHD [40], the first HDC approach for graph classification, encodes graph structure, but does not exploit node attributes, limiting accuracy. NysHD [58] improves accuracy through Nyström approximations; however, it incurs additional propagation kernel cost, relies on uniform landmark sampling leading to redundant landmarks, and does not exploit the sparsity in adjacency and histogram matrices.

FPGA Acceleration of HDC: Prior hardware acceleration efforts for HDC have targeted domains such as biosignals [15], image descriptors [37], and activity recognition [26]. E³-HDC [46] accelerates random-projection encoding; FACH [20] accelerates similarity engines; DistriHD [32] scales HDC across FPGA clusters for image workloads. HyperGraf [9] and [5] apply HDC to graph reasoning tasks. These works validate hardware-accelerated HDC but target different encodings and tasks. To the best of our knowledge, **HyperX** is the first to exploit FPGA to accelerate Nyström-based HDC for graph classification.

8 Conclusion and Future Work

We presented **HyperX**, the first FPGA accelerator for Nyström-based HDC graph classification, by integrating DPP-based landmark sampling, a streaming projection design, $O(1)$ MPH lookups, and statically load-balanced SpMV. Experimental results demonstrate that **HyperX** achieves significantly lower latency and higher energy efficiency compared to CPU and GPU baselines on ZCU104, while *improving* classification accuracy by 3.4% on average compared to prior HDC methods. Looking ahead, we plan to extend these techniques to other graph tasks such as node classification and link prediction.

Acknowledgments

This work is supported by the DEVCOM Army Research Lab (ARL) under grant W911NF-242-0194, and the National Science Foundation (NSF) under grants CSSI-2311870 and OAC-2505107.

References

- [1] Advanced Micro Devices, Inc. 2023. *AXI SmartConnect LogiCORE IP Product Guide (PG247)*. <https://docs.amd.com/r/en-US/pg247-smartconnect> Version 4.1.
- [2] Advanced Micro Devices, Inc. 2024. *AMD Vitis Unified IDE, Version 2024.2*. <https://www.amd.com/en/products/software/adaptive-socs-and-fpgas/vitis/vitis-ide.html> Release 2024.2.
- [3] Advanced Micro Devices, Inc. 2024. *Vitis High-Level Synthesis User Guide (UG1399)*. <https://docs.amd.com/r/en-US/ug1399-vitis-hls> Version 2024.2.
- [4] AMD Xilinx. [n. d.]. *Zynq UltraScale+ MPSoc ZCU104 Evaluation Kit*. <https://www.xilinx.com/products/boards-and-kits/zcu104.html>. Accessed: Sep. 25, 2025.

- [5] Hamza Errahmouni Barkam, Sanggeon Yun, Hanning Chen, Paul Gensler, Albi Mema, Andrew Ding, George Michelogiannakis, Hussam Amrouch, and Mohsen Imani. 2023. Reliable hyperdimensional reasoning on unreliable emerging technologies. In *2023 IEEE/ACM International Conference on Computer Aided Design (ICCAD)*. IEEE, 1–9.
- [6] Karsten M Borgwardt, Cheng Soon Ong, Stefan Schönauer, SVN Vishwanathan, Alex J Smola, and Hans-Peter Kriegel. 2005. Protein function prediction via graph kernels. *Bioinformatics* 21, suppl_1 (2005), i47–i56.
- [7] Cheng-Yang Chang, Yu-Chuan Chuang, Chi-Tse Huang, and An-Yeu Wu. 2023. Recent Progress and Development of Hyperdimensional Computing (HDC) for Edge Intelligence. *IEEE Journal on Emerging and Selected Topics in Circuits and Systems* 13, 1 (2023), 119–136. doi:10.1109/JETCAS.2023.3242767
- [8] Hanning Chen, Yang Ni, Ali Zakeri, Zhuowen Zou, Sanggeon Yun, Fei Wen, Behnam Khaleghi, Narayan Srinivasa, Hugo Latapie, and Mohsen Imani. 2024. HDRReason: Algorithm-Hardware Codesign for Hyperdimensional Knowledge Graph Reasoning. arXiv:2403.05763 [cs.AR] <https://arxiv.org/abs/2403.05763>
- [9] Hanning Chen, Ali Zakeri, Fei Wen, Hamza Barkam, and Mohsen Imani. 2023. HyperGRAF: Hyperdimensional Graph-Based Reasoning Acceleration on FPGA. 34–41. doi:10.1109/FPL60245.2023.00013
- [10] Sohun Datta, Ryan AG Antonio, Aldrin RS Ison, and Jan M Rabaey. 2019. A programmable hyper-dimensional processor architecture for human-centric IoT. *IEEE Journal on Emerging and Selected Topics in Circuits and Systems* 9, 3 (2019), 439–452.
- [11] Asim Kumar Deb Nath, Rosa L Lopez de Compadre, Gargi Deb Nath, Alan J Shusterman, and Corwin Hansch. 1991. Structure-activity relationship of mutagenic aromatic and heteroaromatic nitro compounds. correlation with molecular orbital energies and hydrophobicity. *Journal of medicinal chemistry* 34, 2 (1991), 786–797.
- [12] Paul D Dobson and Andrew J Doig. 2003. Distinguishing enzyme structures from non-enzymes without alignments. *Journal of molecular biology* 330, 4 (2003), 771–783.
- [13] Arpan Dutta, Saransh Gupta, Behnam Khaleghi, Rishikanth Chandrasekaran, Weihong Xu, and Tajana Rosing. 2022. HDnn-PIM: Efficient in Memory Design of Hyperdimensional Computing with Feature Extraction. In *Proceedings of the Great Lakes Symposium on VLSI 2022 (Irvine, CA, USA) (GLSVLSI '22)*. Association for Computing Machinery, New York, NY, USA, 281–286. doi:10.1145/3526241.3530331
- [14] Federico Errica, Marco Podda, Davide Bacciu, and Alessio Micheli. 2022. A Fair Comparison of Graph Neural Networks for Graph Classification. arXiv:1912.09893 [cs.LG] <https://arxiv.org/abs/1912.09893>
- [15] Lulu Ge and Keshab K Parhi. 2021. Seizure detection using power spectral density via hyperdimensional computing. In *ICASSP 2021-2021 IEEE International Conference on Acoustics, Speech and Signal Processing (ICASSP)*. IEEE, 7858–7862.
- [16] Alejandro Hernández-Cano, Namiko Matsumoto, Eric Ping, and Mohsen Imani. 2021. Onlinehd: Robust, efficient, and single-pass online learning using hyperdimensional system. In *2021 Design, Automation & Test in Europe Conference & Exhibition (DATE)*. IEEE, 56–61.
- [17] Binbin Hu, Zhiqiang Zhang, Chuan Shi, Jun Zhou, Xiaolong Li, and Yuan Qi. 2019. Cash-Out User Detection Based on Attributed Heterogeneous Information Network with a Hierarchical Attention Mechanism. *Proceedings of the AAAI Conference on Artificial Intelligence* 33, 01 (Jul. 2019), 946–953. doi:10.1609/aaai.v33i01.3301946
- [18] Mohsen Imani, Yeseong Kim, Sadegh Riazi, John Messerly, Patric Liu, Farinaz Koushanfar, and Tajana Rosing. 2019. A framework for collaborative learning in secure high-dimensional space. In *2019 IEEE 12th International Conference on Cloud Computing (CLOUD)*. IEEE, 435–446.
- [19] Mohsen Imani, Justin Morris, John Messerly, Helen Shu, Yaobang Deng, and Tajana Rosing. 2019. Bric: Locality-based encoding for energy-efficient brain-inspired hyperdimensional computing. In *Proceedings of the 56th Annual Design Automation Conference 2019*. 1–6.
- [20] Mohsen Imani, Sahand Salamat, Saransh Gupta, Jiani Huang, and Tajana Rosing. 2019. FACH: FPGA-based acceleration of hyperdimensional computing by reducing computational complexity (ASPAC '19). Association for Computing Machinery, New York, NY, USA, 493–498. doi:10.1145/3287624.3287667
- [21] Aditya Joshi, Johan T Halseth, and Pentti Kanerva. 2016. Language geometry using random indexing. In *International Symposium on Quantum Interaction*. Springer, 265–274.
- [22] Pentti Kanerva. 2009. Hyperdimensional computing: An introduction to computing in distributed representation with high-dimensional random vectors. *Cognitive computation* 1, 2 (2009), 139–159.
- [23] Jaeyoung Kang, Behnam Khaleghi, Yeseong Kim, and Tajana Rosing. 2022. Xcelhd: An efficient gpu-powered hyperdimensional computing with parallelized training. In *2022 27th Asia and South Pacific Design Automation Conference (ASP-DAC)*. IEEE, 220–225.
- [24] Behnam Khaleghi, Jaeyoung Kang, Hanyang Xu, Justin Morris, and Tajana Rosing. 2022. GENERIC: highly efficient learning engine on edge using hyperdimensional computing. In *Proceedings of the 59th ACM/IEEE Design Automation Conference (San Francisco, California) (DAC '22)*. Association for Computing Machinery, New York, NY, USA, 1117–1122. doi:10.1145/3489517.3530669
- [25] Yeseong Kim, Mohsen Imani, Niema Moshiri, and Tajana Rosing. 2020. Geniehd: Efficient dna pattern matching accelerator using hyperdimensional computing. In *2020 Design, Automation & Test in Europe Conference & Exhibition (DATE)*. IEEE, 115–120.
- [26] Yeseong Kim, Mohsen Imani, and Tajana S Rosing. 2018. Efficient human activity recognition using hyperdimensional computing. In *Proceedings of the 8th International Conference on the Internet of Things*. 1–6.
- [27] Denis Kleyko, Dmitri Rachkovskij, Evgeny Osipov, and Abbas Rahimi. 2023. A survey on hyperdimensional computing aka vector symbolic architectures, part ii: Applications, cognitive models, and challenges. *Comput. Surveys* 55, 9 (2023), 1–52.
- [28] Alex Kulesza. 2012. Determinantal Point Processes for Machine Learning. *Foundations and Trends® in Machine Learning* 5, 2–3 (2012), 123–286. doi:10.1561/22000000044
- [29] Sanjiv Kumar, Mehryar Mohri, and Ameet Talwalkar. 2012. Sampling methods for the Nyström method. *The Journal of Machine Learning Research* 13, 1 (2012), 981–1006.
- [30] Liangzhen Lai and Naveen Suda. 2018. Enabling deep learning at the IoT edge (ICCAD '18). Association for Computing Machinery, New York, NY, USA, Article 135, 6 pages. doi:10.1145/3240765.3243473
- [31] Chengtao Li, Stefanie Jegelka, and Suwit Sra. 2016. Fast DPP Sampling for Nyström with Application to Kernel Methods. doi:10.48550/arXiv.1603.06052
- [32] Dehua Liang, Jun Shiomi, Noriyuki Miura, and Hiromitsu Awano. 2022. DistriHD: A Memory Efficient Distributed Binary Hyperdimensional Computing Architecture for Image Classification. 43–49. doi:10.1109/ASP-DAC52403.2022.9712589
- [33] Antoine Limasset, Guillaume Rizk, Rayan Chikhi, and Pierre Peterlongo. 2017. Fast and scalable minimal perfect hashing for massive key sets. *arXiv preprint arXiv:1702.03154* (2017).
- [34] Fangxin Liu, Haomin Li, Ning Yang, Yichi Chen, Zongwu Wang, Tao Yang, and Li Jiang. 2024. PAAP-HD: PIM-Assisted Approximation for Efficient Hyperdimensional Computing. In *2024 29th Asia and South Pacific Design Automation Conference (ASP-DAC)*. 46–51. doi:10.1109/ASP-DAC58780.2024.10473823
- [35] Alec Lu, Zhenman Fang, Weihua Liu, and Lesley Shannon. 2021. Demystifying the Memory System of Modern Datacenter FPGAs for Software Programmers through Microbenchmarking. In *The 2021 ACM/SIGDA International Symposium on Field-Programmable Gate Arrays (Virtual Event, USA) (FPGA '21)*. Association for Computing Machinery, New York, NY, USA, 105–115. doi:10.1145/3431920.3439284
- [36] Christopher Morris, Nils M. Kriege, Franka Bause, Kristian Kersting, Petra Mutzel, and Marion Neumann. 2020. TUDataset: A collection of benchmark datasets for learning with graphs. arXiv:2007.08663 [cs.LG] <https://arxiv.org/abs/2007.08663>
- [37] Peer Neubert and Stefan Schubert. 2021. Hyperdimensional computing as a framework for systematic aggregation of image descriptors. In *Proceedings of the IEEE/CVF conference on computer vision and pattern recognition*. 16938–16947.
- [38] Marion Neumann, Roman Garnett, Christian Bauckhage, and Kristian Kersting. 2016. Propagation kernels: efficient graph kernels from propagated information. *Machine learning* 102, 2 (2016), 209–245.
- [39] Tony Nowatzki, Vinay Gangadhar, Newsha Ardalani, and Karthikeyan Sankaralingam. 2017. Stream-Dataflow Acceleration. 45, 2 (June 2017), 416–429. doi:10.1145/3140659.3080255
- [40] Igor Nunes, Mike Heddes, Tony Givargis, Alexandru Nicolau, and Alex Veidenbaum. 2022. GraphHD: efficient graph classification using hyperdimensional computing. In *Proceedings of the 2022 Conference & Exhibition on Design, Automation & Test in Europe (Antwerp, Belgium) (DATE '22)*. European Design and Automation Association, Leuven, BEL, 1485–1490.
- [41] NVIDIA Corporation. [n. d.]. NVIDIA System Management Interface (nvidia-smi). <https://developer.nvidia.com/nvidia-system-management-interface>. Accessed: Sept. 2025.
- [42] Tony A Plate. 1995. Holographic reduced representations. *IEEE Transactions on Neural networks* 6, 3 (1995), 623–641.
- [43] Ali Rahimi and Benjamin Recht. 2007. Random features for large-scale kernel machines. *Advances in neural information processing systems* 20 (2007).
- [44] Areen Rasool, Jamshaid Ul Rahman, and Rongin Uwitije. 2025. Enhancing molecular property prediction with quantized GNN models. *Journal of Cheminformatics* 17, 1 (2025), 81.
- [45] Kaspar Riesen and Horst Bunke. 2008. IAM graph database repository for graph based pattern recognition and machine learning. In *Joint IAPR international workshops on statistical techniques in pattern recognition (SPR) and structural and syntactic pattern recognition (SSPR)*. Springer, 287–297.
- [46] Mahboobe Sadeghipour Roodsari, Jonas Krautter, Vincent Meyers, and Mehdi Tahoori. 2024. E3HDC: Energy Efficient Encoding for Hyper-Dimensional Computing on Edge Devices. In *2024 34th International Conference on Field-Programmable Logic and Applications (FPL)*. 274–280. doi:10.1109/FPL64840.2024.00045

- [47] Sahand Salamat, Mohsen Imani, Behnam Khaleghi, and Tajana Rosing. 2019. F5-hd: Fast flexible fpga-based framework for refreshing hyperdimensional computing. In *Proceedings of the 2019 ACM/SIGDA International Symposium on Field-Programmable Gate Arrays*. 53–62.
- [48] Jiawei Shao, Haowei Zhang, Yuyi Mao, and Jun Zhang. 2023. Branchy-GNN: a Device-Edge Co-Inference Framework for Efficient Point Cloud Processing. arXiv:2011.02422 [cs.DC] <https://arxiv.org/abs/2011.02422>
- [49] Guy L Steele Jr and Sebastiano Vigna. 2022. Computationally easy, spectrally good multipliers for congruential pseudorandom number generators. *Software: Practice and Experience* 52, 2 (2022), 443–458.
- [50] Jeffrey J Sutherland, Lee A O'Brien, and Donald F Weaver. 2003. Spline-fitting with a genetic algorithm: A method for developing classification structure- activity relationships. *Journal of chemical information and computer sciences* 43, 6 (2003), 1906–1915.
- [51] Anthony Thomas, Sanjoy Dasgupta, and Tajana Rosing. 2021. A theoretical perspective on hyperdimensional computing. *Journal of Artificial Intelligence Research* 72 (2021), 215–249.
- [52] Nikil Wale, Ian Watson, and George Karypis. 2008. Comparison of Descriptor Spaces for Chemical Compound Retrieval and Classification. *Knowl. Inf. Syst.* 14 (03 2008), 347–375. doi:10.1109/ICDM.2006.39
- [53] Thomas Wang. 1997. Integer Hash Functions. <https://web.archive.org/web/20071223173210/http://www.concentric.net/~Ttwang/tech/inthash.htm>. Accessed: 2025-09-12.
- [54] Christopher Williams and Matthias Seeger. 2000. Using the Nyström method to speed up kernel machines. *Advances in neural information processing systems* 13 (2000).
- [55] Samuel Williams, Andrew Waterman, and David Patterson. 2009. Roofline: An Insightful Visual Performance Model for Multicore Architectures. *Commun. ACM* 52, 4 (April 2009), 65–76. doi:10.1145/1498765.1498785
- [56] Pinar Yanardag and S.V.N. Vishwanathan. 2015. Deep Graph Kernels. In *Proceedings of the 21th ACM SIGKDD International Conference on Knowledge Discovery and Data Mining* (Sydney, NSW, Australia) (*KDD '15*). Association for Computing Machinery, New York, NY, USA, 1365–1374. doi:10.1145/2783258.2783417
- [57] Quanling Zhao, Kai Lee, Jeffrey Liu, Muhammad Huzaifa, Xiaofan Yu, and Tajana Rosing. 2022. FedHD: federated learning with hyperdimensional computing. In *Proceedings of the 28th Annual International Conference on Mobile Computing And Networking* (Sydney, NSW, Australia) (*MobiCom '22*). Association for Computing Machinery, New York, NY, USA, 791–793. doi:10.1145/3495243.3558757
- [58] Quanling Zhao, Anthony Hitchcock Thomas, Ari Brin, Xiaofan Yu, and Tajana Rosing. 2025. Bridging the Gap Between Hyperdimensional Computing and Kernel Methods via the Nyström Method. *Proceedings of the AAAI Conference on Artificial Intelligence* 39, 21 (Apr. 2025), 22813–22821. doi:10.1609/aaai.v39i21.34442
- [59] Ao Zhou, Jianlei Yang, Tong Qiao, Yingjie Qi, Zhi Yang, Weisheng Zhao, and Chunming Hu. 2024. Graph Neural Networks Automated Design and Deployment on Device-Edge Co-Inference Systems. In *Proceedings of the 61st ACM/IEEE Design Automation Conference* (San Francisco, CA, USA) (*DAC '24*). Association for Computing Machinery, New York, NY, USA, Article 187, 6 pages. doi:10.1145/3649329.3655938
- [60] Zhuowen Zou, Yeseong Kim, Farhad Imani, Haleh Alimohamadi, Rosario Cammarota, and Mohsen Imani. 2021. Scalable edge-based hyperdimensional learning system with brain-like neural adaptation. In *Proceedings of the International Conference for High Performance Computing, Networking, Storage and Analysis*. 1–15.